Published in final edited form as:
Magn Reson Med. 2010 January ; 63(1): 41–50. doi:10.1002/mrm.22158.

Helium-3 MR q-space Imaging with Radial Acquisition and Iterative Highly Constrained Back-Projection

Rafael L. O'Halloran[1], **James H. Holmes**[1], **Yu-Chien Wu**[2,3], **Andrew Alexander**[1], and **Sean B. Fain**[1,2,4]

[1]Department of Medical Physics; University of Wisconsin, Madison

[2]Department of Radiology, University of Wisconsin, Madison

[3]Waisman Laboratory for Brain Imaging and Behavior, University of Wisconsin, Madison

[4]Department of Biomedical Engineering; University of Wisconsin, Madison

Abstract

An under-sampled diffusion weighted stack-of-stars acquisition is combined with iterative highly constrained back-projection to perform hyperpolarized He-3 MR q-space imaging with combined regional correction of RF- and T_1-related signal loss in a single breath-held scan. The technique is tested in computer simulations and phantom experiments and demonstrated in a healthy human volunteer with whole lung coverage in a 13 s breath-hold. Measures of lung microstructure at 3 different lung volumes are evaluated using inhaled gas volumes of 500 mL, 1000 mL, and 1500 mL to demonstrate feasibility. Phantom results demonstrate that the proposed technique is in agreement with theoretical values as well as with a fully sampled 2D Cartesian acquisition. Results from the volunteer study demonstrate that the root mean squared diffusion distance increased significantly from the 500 mL volume to the 1000 mL volume. This technique represents the first demonstration of a spatially resolved hyperpolarized He-3 q-space imaging technique and shows promise for microstructural evaluation of lung disease in three dimensions.

Keywords

HYPR; Iterative Reconstruction; Projection Imaging; MRI; Helium-3; Diffusion; q-space; hyperpolarized gases

Introduction

In hyperpolarized (HP) He-3 MRI, diffusion-weighted (DW) methods have proven useful in evaluating the progression of degenerative lung diseases such as emphysema [1,2] as well as for detecting early emphysematous changes in asymptomatic smokers [3]. Due to breath-hold time limitations, the conventional approach to DW HP He-3 imaging is to acquire one diffusion-weighted image and one non-diffusion-weighted image and to calculate the apparent diffusion coefficient (ADC). A potential drawback of this approach is that the ADC depends on the level of diffusion weighting applied. Q-space imaging (QSI) [4] is a generalization of ADC imaging in which images acquired at multiple diffusion weightings are used to compute diffusion probability profiles. This provides a measurement of the level of restriction independent of the diffusion weightings used. However, due to the longer scan

Correspondence and reprint requests: Sean B. Fain J5/M158 CSC Medical Physics 600 Highland Avenue Madison, WI 53792 Phone 608 263-0090; Fax 608 265-9840; sfain@wisc.edu.

times needed to acquire multiple DW images and sensitivity to motion, QSI has typically been limited to neuro-MRI applications such as for resolving the orientations of crossing white matter tracks in the brain [5].

Recently, QSI has also been applied to HP He-3 NMR spectra acquired over the whole human lung [6]. A bi-Gaussian function was shown to fit the measured displacement probability profile. It was noted that the measured root mean squared (RMS) values of smaller and larger Gaussian terms correlated well with previously reported average diameters of alveoli and terminal and respiratory bronchioles respectively. Moreover, a recent proposed modification to the QSI diffusion model [7] that accounts for the short diffusion time condition ($\Delta \approx \delta$) has been shown to give accurate measurements in the case of free Gaussian diffusion and improved measurements compared to the unmodified analysis in the case of restricted diffusion. This suggests that it may be possible to obtain measurements of microscopic lung structures with QSI. However, the constraints of imaging within a breath-hold and with finite HP magnetization have prevented this technique from being applied to spatially-resolved HP He-3 imaging of the lung *in vivo*.

To meet these challenges, a radially under-sampled stack-of-stars acquisition combined with an iterative constrained reconstruction is proposed. Under-sampling in k-space allows the acquisition of fewer k-space lines per reconstructed image [8]. This reduces both scan time and the amount of magnetization needed per image. However, as the level of under-sampling increases, the amount of streak artifact is also expected to increase.

The highly constrained back-projection reconstruction (HYPR) was shown to mitigate streak artifact in the presence of angular under-sampling in sparse image data such as dynamic contrast enhanced angiography [9]. The success of HYPR in accelerated angiography using undersampled projection acquisition is the motivation for applying it to HP He-3 QSI of the lung. However, DW HP He-3 MRI of the human lung presents a greater challenge to the HYPR reconstruction than angiography due to decreased spatial and parametric (i.e. time or diffusion weighting) sparsity. Unlike angiographic images, which have relatively few vascular structures in the field of view that enhance gradually in time, DW HP He-3 images contain signal throughout the lungs that may change abuptly with each diffusion weighting.The iterative HYPR (I-HYPR) reconstruction [10], has been shown to be more robust to decreased sparsity. Therefore, in the present work, I-HYPR is used in order to reconstruct more accurate quantitative parametric images from the under-sampled data.

In this work, the undersampled q-space methodology is tested in computer simulations and phantom experiments. Feasibility is demonstrated in a healthy human volunteer for 3D QSI in a 13 s breath-hold that includes simultaneous correction for signal loss due to RF and T_1 over the duration of the breath-hold.

Theory

q-space

QSI is performed by acquiring images of an object with multiple diffusion weightings. The degree of diffusion weighting can be expressed by a b-value and depends on the shape and size of the diffusion sensitizing gradient pulse. For a bi-polar trapezoidal pulse (Fig 1), the b-value, *b*, is given by [11]

$$b=\gamma^2 G_D^2 \cdot \left[\delta^2\left(\Delta-\frac{\delta}{3}\right)+\varepsilon\left(\delta^2-2\Delta\delta+\Delta\varepsilon-\frac{7}{6}\delta\varepsilon+\frac{8}{15}\varepsilon^2\right)\right] \quad [1]$$

where γ is the gyromagnetic ratio, G_D is the diffusion gradient strength, ε is the ramp time, δ is the pulse duration of a single lobe, and Δ is the time between the beginning of the first lobe and the beginning of the second, also known as the diffusion time. Alternatively, diffusion weighting for a bi-polar trapezoidal pulse can be specified by a vector, $\vec{q}$, given by [12]:

$$\vec{q} = \frac{\gamma G_D}{2\pi} (\delta - \varepsilon) \hat{G}_D, \quad [2]$$

where $\hat{G}_D$ is a unit vector pointing in the direction of the diffusion weighting gradient. Let the expected value of the measured signal at a particular $\vec{q}$ and for a given diffusion time, Δ, normalized by the non-diffusion-weighted signal be $E\left[\vec{q}, \Delta\right]$. Now $E\left[\vec{q}, \Delta\right]$ is given by the integral:

$$E\left[\vec{q}, \Delta\right] = \int DPP\left[\vec{R}, \Delta\right] \exp\left[i2\pi\vec{q} \cdot \vec{R}\right] d\vec{R}, \quad [3]$$

where the probability that a spin will undergo a displacement $\vec{R}$ in the diffusion time, Δ, is defined as the diffusion probability profile, $DPP[\vec{R}, \Delta]$, and the frequency coefficient of the complex term depends on the projection of the displacement vector onto $\vec{q}$. Note that $\vec{q}$ has units of inverse length and is the Fourier conjugate variable to the average displacement vector $\vec{R}$. Thus, the DPP can be calculated by performing the Fourier transform on the measured DW signal.

The key assumption needed for Eq [3] to hold is that the width of the diffusion pulse be much smaller than the diffusion time (δ<<Δ). This ensures that nearly all of the measured diffusion takes place between the diffusion pulses and not during them. This assumption, in the interest of performing QSI in a short breath-hold scan, is clearly violated for the bipolar trapezoidal pulse where δ=Δ (Fig 1). Violating this assumption results in a measured DPP that is narrower than the ideal DPP of the system [13,14,15]. A recent proposed modification to the QSI methodology has been shown to give accurate measured DPP's in the case of free Gaussian diffusion and improved measured DPP's compared to the unmodified analysis in the case of restricted diffusion [7]. Two modifications are given. First, the q-values are multiplied by a constant factor depending on the relative values of Δ and δ according to

$$\vec{q}_{\text{mod}} = \vec{q} \sqrt{\frac{\Delta - \delta/3}{\Delta + \delta}}. \quad [4]$$

Second, the results should be interpreted at the experimental diffusion time, t_{exp}, given by,

$$t_{exp} = \Delta + \delta. \quad [5]$$

In this work, computations will be performed using the modified values given by Eq [4] and Eq [5].

Iterative HYPR

Details of the I-HYPR reconstruction have been published previously [10]. Briefly, I-HYPR applies constrained reconstruction based on a maximum-likelihood approach to reconstruct a parametric series of images from radially undersampled projection data. The radially undersampled reconstruction problem is addressed by using a constraining image reconstructed from data gathered from all or part of the parametric space. To enforce consistency with the measured data, the measured projections are normalized by synthesized projections of the constraining image at the identical projection angles to form a ratio sinogram. This ratio sinogram is reconstructed with unfiltered back-projection and the resulting image is multiplied by the constraining image to produce a new estimate of the image. The new estimate is taken to be the constraining image for the next iteration and the process is repeated.

Methods

To demonstrate the accuracy of the I-HYPR reconstruction on DW data, it was first tested using a simulation synthesized from data acquired using a DW Cartesian sequence. The acquisition and reconstruction methods were then tested in phantom experiments for a full q-space experiment using multiple b-value weightings acquired within a rapid 3D acquisition designed for single breath-hold imaging. Finally, the experimental sequence and reconstruction were tested in a normal human subject undergoing different inflation lung volumes to establish quantitative agreement with previous studies and demonstrate expected qualitative changes in alveolar and small airway structures as a function of lung volume.

Simulation

To demonstrate the feasibility of calculating quantitative parametric maps in the lungs using I-HYPR, a radial DW He-3 MR data set was simulated from He-3 MR images acquired with a Cartesian trajectory. Sinogram data were synthesized by performing the Radon transform on the weighted and unweighted images from a single 128×128 pixel slice positioned in a region of known gas trapping using 200 angles for the unweighted image and trials of 4, 8, 16, 32, and 200 angles for the weighted image. To simulate realistic levels of noise, independent realizations of zero mean Gaussian noise with varying standard deviation were added in quadrature to the sinogram. The noisy sinogram was then calculated by taking the square root of the sum of the 2 squared channels. The unweighted image was calculated by filtered back-projection (FBP). The weighted images were calculated with I-HYPR and FBP for comparison. Apparent diffusion coefficient maps were calculated by:

$$ADC = -\frac{1}{b}\ln\left(\frac{S_{DW}}{S_0}\right) \quad [6]$$

where S_{DW} and S_0 are the diffusion weighted and unweighted signals respectively and b is the b-value (1.6 s/cm^2). To compare the noise levels in the simulations, the noise level was quantified by dividing the standard deviation of a region in the background of the sinogram by the mean value of the entire sinogram and multiplying by 100. These values are reported as percent noise.

To quantitatively evaluate the errors in the DW images reconstructed with I-HYPR and the corresponding ADC maps, they were compared to the fully-sampled noise-free FBP-reconstructed DW image and the corresponding ADC map. The percent root-mean-square (RMS) difference between the DW images reconstructed with I-HYPR and the fully-sampled FBP image was computed over the region of support of the object for each noise

level and number of simulated angles. Restricting the calculation to the region of support eliminates the influence of pixels in the noise background with very low signal values. The RMS difference in the ADC images was also calculated in this way. Additionally, the mean and standard deviation in two separate 10×10 pixel regions of interest (ROI) were computed for each noise level and number of simulated angles in both the DW and ADC images.

Phantom Construction

The phantom experiments were carefully designed to test the ability of the technique to measure expected diffusion dimensions for different levels of restriction ranging from unrestricted, partially restricted, to fully restricted. Two phantoms were constructed from 5 cm inner diameter PVC pipe sealed at both ends with end-caps. One end-cap on each of the phantoms had a hole fitted with 1/8”-inner-diameter Tygon tube (US Plastic Corp., Lima, OH, USA) to allow evacuation and filling. Phantom 1 contained a piece of synthetic foam cut in the shape of a half-cylinder to occupy half of the space in the phantom for a net volume of 180 cc. The average separation of structures in the foam was estimated with high resolution optical scanning by measuring the approximate diameter of 20 of the circular structures in the scanner image (Fig 2a). The approximate separation was found to be 270 ± 60 μm (Fig 2). It should also be noted that the pores in the foam material are highly connected and do not provide complete restriction of the gas. Phantom 2 contained a stack of 290 μm thick acetal plastic plates separated by one plate thickness (Fig 3). However the plate separation was not completely uniform due to deflection of the thin plates (Fig 3c) and was measured with high resolution optical scanning to be 280 ± 100 μm.

HP Gas Production

HP ^{3}He gas was polarized using a prototype commercial spin-exchange optical pumping polarizer (HeliSpin, GE Healthcare, Milwaukee, WI) to polarize ^{3}He to 30–40%. For human studies a “dose” of HP ^{3}He was prepared by drawing ^{3}He into a Tedlar plastic bag (Jensen Inert Inc., Coral Springs, FL, USA) from the polarizing unit. The Tedlar bag was purged and rinsed with nitrogen prior to filling to prevent oxygen contamination. The desired volume was obtained by adding nitrogen to the bag. For phantom studies, the ^{3}He was drawn from the polarizing unit directly into the phantom via an attached 1/8”-diameter Tygon tube (US Plastic Corp., Lima, OH, USA). Phantoms were evacuated and purged with nitrogen several times before filling with ^{3}He to 1.0 ± 0.1 atm.

Hyperpolarized He-3 MRI

Diffusion-weighted hyperpolarized He-3 MRI was performed on the phantoms and a healthy volunteer using a 1.5 T MR scanner (Signa HDx, GE Healthcare, Milwaukee, WI) with a transmit/receive chest RF coil tuned to the He-3 resonant frequency. Scans were performed over a 3D volume consisting of 8 axial slices at a 3 cm thickness, FOV = 42 cm, ±62.5 kHz BW, nominal flip angle of 2° and in-plane resolution of 3.3 mm^2 using a fast-GRE 3D stack-of-stars sequence with radial acquisition in the axial plane and conventional phase encoding in the superior-inferior (z-axis) direction [8]. All phase encodes for a given projection were acquired before proceeding to the next projection. Phase-encoding was chosen over 2D multi-slice excitation in order to reduce the scan time using a short duration non-selective RF pulse. A total of 256 unique projection angles were acquired per phase encode with 16 projections acquired per each of the 8 non-zero q-values and 16 projections without diffusion weighting acquired between each set of progressively decreasing diffusion-weighted projections (Fig. 4). Non-weighted projections were acquired at intervals evenly interspersed throughout the breath-hold to correct the diffusion weighted data for signal loss due to flip angle and T_1-decay as described later. Diffusion-encoding pulses were bipolar trapezoidal pulses oriented along the z-axis (Fig 1).

Two different Signa HDx 1.5 T scanners were used to perform the experiments. Due to differences in the maximum achievable gradient strength on the two scanners, the human volunteer and phantom 1 were scanned with different parameters than phantom 2. For the volunteer and phantom 1, the maximum diffusion gradient strength, G_d, was 3.2 G/cm resulting in q-values ranging from 0.18 to 1.5 mm^{-1} (q_{mod} = 0.10 to 0.84 mm^{-1}), ε = 300 μs, δ = 1700 μs, Δ = 1700 μs, TR/TE = 6.1 / 4.2 ms, and total scan time 13 s. For phantom 2, the maximum diffusion gradient strength, G_d, was 1.9 G/cm resulting in q-values ranging from 0.15 to 1.2 mm^{-1} (q_{mod} = 0.088 to 0.71 mm^{-1}), ε = 300 μs, δ = 2300 μs, Δ = 2300 μs, TR/TE = 7.2 / 5.4 ms, and a total scan time of 15 s.

To verify the accuracy of the 3D acquisition and reconstruction in comparison to a conventional fully sampled Cartesian method, an additional set of eight 2D fast-GRE diffusion-weighted (DW) hyperpolarized He-3 MRI scans of phantom 1 were acquired. Each of the eight 2D images was acquired at a q-value corresponding to the 8 q-values acquired in the 3D scan. The 2D scans were performed on a single 3 cm thick slice with 20 cm FOV, 256 × 256 image matrix, and 10° flip angle.

The human subject experiment was approved by our IRB and performed under IND#64867. To investigate the effect of varying the inhaled volume on q-space results, the human volunteer underwent MRI following inhalation of a gas mixture consisting of 400 mL He-3 at 30% polarization mixed with different volumes of nitrogen (100 mL, 600 mL, and 1100 mL) for a total of 3 scans with total inhaled gas volumes of 500 mL, 1000 mL, and 1500 mL.

Reconstruction

Each set of 16 consecutively acquired angles were reconstructed using I-HYPR resulting in 8 unweighted and 8 diffusion weighted images for each of the 8 slices for a total of 128 images per scan. Iteration was terminated after the RMS difference between the sinograms of the reconstructed images and the measured data ceased to decrease or after 50 iterations, whichever condition was met first. The constraining images were reconstructed using all 256 unique projections acquired for a given slice.

RF and T_1 correction

To obtain quantitative diffusion measurements it is necessary to correct for the confounding effect of signal loss due to the applied RF pulse and T_1. This correction must be performed pixel-wise due to the inhomogeneity of the B_1 field for the flexible RF-coil design used, which wraps snugly around the chest. To obtain a correction map, the signal in each pixel from the 8 unweighted images, S_n, was fit to the model [6]:

$$S_n = S_0 \cdot K^n, \quad [7]$$

where S_0, is the signal in the first image and n is the number of RF pulses applied between S_0 and S_n and K is a constant that can be modeled as,

$$K = \cos(\alpha)\exp(-TR/T_1), \quad [8]$$

where α is the flip angle, TR is the repetition time and T_1 is the relaxation time, dominated by the effect of paramagnetic molecular oxygen. The signal intensities for all images were then corrected by inverting Eq. [7].

Data Analysis

Using the modified q-values, q_{mod}, the normalized signal intensity $E\left[\vec{q}_{\mathrm{mod}},\Delta\right]$ was calculated by dividing the diffusion weighted images by the unweighted images, where the unweighted images were the average of the 8 flip-angle-corrected unweighted images for each slice. The $E\left[\vec{q}_{\mathrm{mod}},\Delta\right]$ was then fit to the Gaussian model:

$$E\left[\vec{q}_{\mathrm{mod}},\Delta\right]=Z\exp\left(-2\pi {X_{RMS}}^2{\vec{q}_{\mathrm{mod}}}^2\right), \quad [9]$$

where X_{RMS} is the RMS width of the DPP. This is equivalent to taking the Fourier transform of $E\left[\vec{q}_{\mathrm{mod}},\Delta\right]$ to obtain the DPP and fitting to:

$$DPP(x)=Z\exp\left(-0.5\cdot\left(\frac{x}{X_{RMS}}\right)^2\right). \quad [10]$$

Fitting to Eq [9], however, is preferred because this approach is more robust to apodization error caused by the limited region sampled in q-space. Note that in the present work a single Gaussian model is used instead of a the bi-Gaussian model used in the previous work of Shanbhag et al. [6]. This is because the 4 parameter bi-Gaussian model would not provide a robust fit to the 8 data points used for the fitting in this study.

Theoretical X_{RMS} values for unrestricted Gaussian diffusion were calculated using the experimental diffusion time, t_{exp}, and the relation,

$$X_{\mathrm{RMS}}=\sqrt{2Dt_{\mathrm{exp}}} \quad [11]$$

with the diffusion coefficient of pure helium, D = 1.9 cm^2/s [16] for comparison with phantom experiments and the diffusion coefficient of helium diluted in air, specifically D = 0.88 cm^2/s, for comparison with the volunteer scans. For restricted diffusion in the phantoms and lung parenchyma in the human volunteer, X_{RMS} values were compared with the known average dimensions of the acetate plates, the foam, and values for alveolar and small airway dimensions in the literature [17].

Results

Simulation

The DW spin density images reconstructed using I-HYPR are compared in Figure 5a to the DW images reconstructed using FBP for each respective noise level. Because the constraining image used is the unweighted image, the anatomy appears to be well represented in all cases, although structured artifacts resembling streaks are more apparent in the most extreme case of radial undersampling (4 projections), particularly as noise level increases.

Fig 5b shows the ADC maps computed with the diffusion weighted images in Fig 5a. The effects of undersampling and noise stemming from the reconstruction error are more apparent in the ADC maps than in the DW images. To evaluate the accuracy of the undersampled reconstruction, the ADC maps calculated from the images reconstructed using I-HYPR are compared with those using FBP reconstruction with 200 equally spaced

projection angles. Two expected trends are apparent. The noise and artifact level in the reconstruction increases with the level of noise in the projection data from top to bottom, and the level of streak artifact decreases as the number of sampled angles increases from left to right. Importantly, the I-HYPR maps are qualitatively the same as the exact FBP result using as few as 16 projection angles. This robustness of I-HYPR to angular undersampling can be exploited to accelerate acquisition speed, while retaining accuracy for diffusion measures. Finally, note that a small amount of spatial blurring is also observed due to the linear interpolation used in the Radon transform. The white box indicates the empirically selected level of angular undersampling chosen for the subsequent human volunteer studies.

In Fig 6 the percent RMS difference between the DW images reconstructed with I-HYPR and the fully-sampled noise-free FBP-reconstructed image are plotted versus the noise-level in varying numbers of angular undersampling (Fig 6a). In all cases the error was below ten percent. For noise levels below 15 % and for 16 or greater simulated angles the error was below 5 percent. Fig 6b shows a similar plot for the ADC maps calculated with I-HYPR-reconstructed DW images. The errors in the ADC images are greater than that in the DW images due to the logarithm operation performed in calculating the ADC (Eq [6]). Note that in the limiting case of zero added noise and full angular sampling there is still approximately 2 percent difference between the DW images reconstructed with IHYPR and the DW image reconstructed with FBP. This is due to the fact that the IHYPR reconstruction is fundamentally a statistical reconstruction and is not an exact reconstruction such as FBP. The approximate nature of the reconstruction manifests itself in the ADC maps as increased noise and, in cases of extreme undersampling, as structured artifacts.

The mean and standard deviations of both the DW image and the ADC map in the 2 ROIs considered are given in Table 1. For both the DW image and the ADC map the means of the I-HYPR reconstructions compare quite well with those in the fully sampled FBP image. Without noise, the standard deviations of the ROIs in the I-HYPR images are comparable to those in the FBP image without noise. As expected the standard deviations were observed to increase with increased added noise.

Phantom Studies

The phantom experiment results are summarized in Table 2 and Fig 7. The free and restricted diffusion regions were each segmented by visual inspection. X_{RMS} measured in the free diffusion region of phantom 1 for the conventional 2D Cartesian technique and the new proposed 3D stack-of-stars experiments were 1200 ± 200 μm and 1170 ± 20 μm respectively (Table 2). These values are in good agreement with the theoretical values for X_{RMS} for unrestricted Gaussian diffusion of 1140 μm calculated with Eq [10] using the experimental diffusion time t_{exp} = 3400 μs and D = 2.05 cm^2/s. The measured signal for the free diffusion region in the conventional 2D and the 3D radial cases compares well with the theoretical expected values for the signal attenuation from unrestricted Gaussian diffusion below about q_{mod} = 0.5 mm^{-1} (Fig 7b, dotted line).

X_{RMS} measured in the foam region of phantom 1 from the conventional 2D Cartesian and proposed 3D stack-of-stars acquisitions were 800 ± 100 μm and 840 ± 10 μm respectively (Table 2). These values are substantially greater than the measured average pore size in the phantom of 270 ± 60 μm, however this discrepancy is expected given the fact that the pores in the foam material are highly connected and therefore do not represent a completely restricted diffusion boundary to the gas. As a comparison to conventionally fully sampled data, the log of the normalized diffusion attenuated signal for the 2D and proposed 3D acquisitions are compared across the measured range of q-values for ROI's placed in the foam region (Fig 7b) and in the free diffusion region (Fig 7c). Measured signal values for the nine separate 2D conventional Cartesian acquisition (circles) lie within errors of the

measured signal values for the single 3D undersampled radial stack of stars acquisition (line).

X_{RMS} measured in the free diffusion region of phantom 2 for the proposed 3D stack-of-stars experiments was 1390 ± 80 μm (Table 2). This value is in good agreement with the theoretical value for X_{RMS} for unrestricted Gaussian diffusion of 1320 μm calculated with Eq [10] using the experimental diffusion time t_{exp} = 4600 μs and D = 2.05 cm^2/s. Note that the theoretical value for free diffusion differs from that in phantom 1 due to the longer diffusion time, Δ, required by the MR scanner gradients for the experiment with phantom 2. X_{RMS} measured in the restricted region of phantom 2 from the proposed 3D stack-of-stars acquisition was 126 ± 40 μm (Table 2). This compares well with the ideal X_{RMS} value of 118 μm predicted for an infinitely restricted 290 μm wide gap as well as the measured value of 110 ± 40 μm that corresponds to the measured gap dimension of 275 ± 100 μm.

Human Volunteer

In Fig 8a, corrected maps of X_{RMS} are shown for each inhaled volume in the human volunteer exam. A decrease in X_{RMS} from anterior to posterior can be observed on the corrected X_{RMS} maps from each of the three inhaled volumes (Fig 8a). This is the expected dependence due to the effect of gravity as the volunteer was in the supine position for imaging. A decrease in X_{RMS} from the apex to base of the lung is also apparent in each of the three volumes.

Figure 8b depicts the regional distribution of the correction factor, K, for each of the inhaled volumes. The correction maps are qualitatively similar for each volume (Fig 8b) with lower values of K observed in the central slices and higher values of K in the apical and basal slices. This dependence is due to the coil sensitivity profile. The small regional differences observable are to be expected because the sensitivity profile of the flexible coil depends on the position of the volunteer's chest and hence on the inhaled volume. Moreover, the regional distribution of oxygen partial pressure likely varies slightly between each inhaled volume.

Plots of X_{RMS} measured in ROIs covering the entire right and left lung parenchyma demonstrate the dependence of inhaled volume on apical to basal position (Fig 9). The difference in the measured X_{RMS} between the 1500 mL volume and the 500 mL volume was approximately 22 μm, while the difference between X_{RMS} in the 1500 mL volume and the 1000 mL volume did not appear to be significant. As an internal comparison to theory, the X_{RMS} values measured in ROI's containing the trachea were 780 ± 40 μm, 790 ± 60 μm, and 780 ± 40 μm for the 500 mL, 1000 mL, and 1500 mL inhaled volumes respectively. These values are in good agreement with the theoretical X_{RMS} calculated for unrestricted Gaussian diffusion of 774 μm, the experimental diffusion time t_{exp} = 3400 μs, and D = 0.88 cm^2/s using Eq [10]. Single pixel profiles though the X_{RMS} maps for each inhaled volume are compared in Fig. 9c. Fig 8a depicts the position of the profile (red dashed line). The decrease in X_{RMS} from anterior to posterior is apparent in each slice. Also note the general increase in X_{RMS} value from the 500 mL volume (solid line) to the 1000 mL and 1500 mL volumes (dashed and dotted lines respectively).

Discussion

This work demonstrates the feasibility of spatially resolved 3D QSI of human lung airspaces *in vivo*. This application of QSI in a 13 s scan was enabled by radial undersampling and the I-HYPR constrained reconstruction. Without accelerated acquisition, these measurements could not be performed in a reasonable breath-hold time. The I-HYPR reconstruction was tested in computer simulations and shown to provide accurate diffusion weighted images

given the unweighted image as a constraining image. Phantom experiments demonstrated that the accelerated 3D QSI technique provides the same X_{RMS} values as a 2D Cartesian technique while enabling volume coverage. The RMS dimensions of the airspaces in a healthy human volunteer showed a dependence on inhaled volume, apical to basal, and anterior to posterior position in the lungs, and values agreed with previously published work [6].

Whole lung averages of the X_{RMS} for all inhaled volumes agree with the previously published results by Shanbhag et al. They reported a weighted average of the measured X_{RMS} over the two fitted Gaussian components in healthy adults to be 333 ± 27 μm. This compares well to the values in Table 3 which were calculated by averaging X_{RMS} values obtained from single Gaussian fits over the entire lung. Note that the effect of changing the inhaled volume on the X_{RMS} is not significant at the whole volume level and can only be appreciated in the spatially resolved measurements.

Testing of the method in phantom experiments ranging from unrestricted to intermediate and highly restricted diffusion provided further support for the validity of the method. The modified q-space theory presented by Lori et al [7] improved the accuracy of measurements of X_{RMS} based on modified q-values. Moreover, the concept of the experimental diffusion time, t_{exp}, from this same work aided in validating the present work by providing the correct diffusion time for the calculation of the expected free diffusion coefficients. The measured X_{RMS} for the free diffusion coefficient in the phantoms at two distinct diffusion times and the measured X_{RMS} in the trachea of the human volunteer were all in agreement with theory when calculated using t_{exp}. The X_{RMS} values measured in the restricted region of phantom 2, the acetal plastic plate phantom, are also in agreement with predicted values providing further validation of the methodology in the opposite regime of complete restriction along the measurement axis.

There are previously reported results in the literature on the effect of inhalation volume on lung microstructure size. In a rat model of emphysema the ADC was shown to be greater after inhaling gas than at functional residual capacity [18]. The observed effect was greater in control rats. Similarly it has been reported that the ADC in healthy human volunteers increased when the inhaled volume increased from 6% total lung capacity to 15% total lung capacity [19]. However, a microscopy study of canine lung *in vivo* found that the number of alveoli in the microscope field increased with the inhaled volume, while the size of the alveoli remained fairly constant over a range of lung volumes from 20% to 80% of TLC [20]. This led to the interpretation that as the inhaled volume increased, alveoli that were previously closed suddenly opened, accounting for the increased lung volume.

In the present study an average increase in X_{RMS} over the whole lung of approximately 6.5 % was observed when the inhaled volume increased from 500 mL to 1500 mL. If this increase is due strictly to balloon-like stretching of the airspaces, and a functional residual capacity of 3 L is assumed, then the expected percent increase in alveolar length scale over this range is about 9%.

$$100 \cdot \left[\left(\frac{3L+1.5L}{3L+0.5L} \right)^{\frac{1}{3}} - 1 \right] \approx 9\% \qquad [12]$$

Given that the observed increase in X_{RMS} of 6.5 % is significantly lower than the 9 % predicted by the expansion model, it is reasonable to speculate that alveolar recruitment may be taking place during inhalation. One possible explanation for this observation is that some

stretching of the airspaces is occurring. Another is that additional paths of communication become available as neighboring alveolar units are recruited.

It is also interesting to note that most of the dependence is measured between 500 mL and 1000 mL followed by very little change from 1000 mL to 1500 mL. This latter observation suggests that there may be a threshold lung volume beyond which there is limited change in the dimensions of the microstructural components of the lungs. Future work will explore these mechanics on a larger population of normal and asthmatic subjects, including pediatric patients.

Conclusions

The first 3D method for *in vivo* hyperpolarized He-3 QSI of the human lung was presented and tested in phantom experiments and in computer simulations. The presented QSI method was completed within a 13 s breath-hold by using an accelerated acquisition with under-sampled radial stack-of-stars k-space sampling in combination with the I-HYPR reconstruction. Measured X_{RMS} values were found to increase as the inhaled gas volume increased from 500 mL to 1500 mL in a healthy volunteer. Future work includes examination of diseased populations such as asthma and emphysema with the QSI technique. In particular the examination of small scale structures in regions of gas trapping in asthma and fibrotic lung disease represent interesting future directions for this work.

Acknowledgments

Funding: Award to SBF from the Sandler Program for Asthma Research.

References

[1]. deLange EE, Mugler JP III, Brookeman JR, Knight-Scott J, Truwit JD, Teates CD, Daniel TM, Bogorad PL, Cates GD. Lung Air spaces: MR imaging evaluation with hyperpolarized 3He Gas. Radiology 1999;210:851–857. [PubMed: 10207491]

[2]. Saam BT, Yablonskiy DA, Kodibagkar VD, Leawoods JC, Gierada DS, Cooper JD, Lefrak SS, Conradi MS. MR Imaging of Diffusion of ^{3}He Gas in Healthy and Diseased Lungs. MRM 2000;44:174–179.

[3]. Fain SB, Panth SR, Evans MD, Wentland AL, Holmes JH, Korosec FR, O'Brien MJ, Fountaine H, Grist TM. Early Emphysematous Changes in Asymptomatic Smokers: Detection with ^{3}He MR Imaging. Radiology 2006;239:875–883. [PubMed: 16714465]

[4]. Callaghan PT, Eccles CD, Xia Y. NMR Microscopy of Dynamic Displacements: k-space and q-space imaging. J Phys E Sci Instrum 1988;21:820–822.

[5]. Tuch DS, Reese TG, Wiegell MR, Wedeen VJ. Diffusion MRI of Complex Neural Architechture. Neuron 2003;40:885–895. [PubMed: 14659088]

[6]. Shanbhag DD, Altes TA, Miller GW, Mata JF, Knight-Scott J. q-space Analysis of Lung Morphology *In-Vivo* with Hyperpolarized ^{3}He Spectroscopy. JMRI 2006;24:84–94. [PubMed: 16767705]

[7]. Lori NF, Conturo TE, Le Bihan D. Definition of Displacement Probability and Diffusion Time in q-space Magnetic Resonance Measurements That Use Finite-Duration Diffusion-Encoding Gradients. JMR 2003;165:185–195. [PubMed: 14643700]

[8]. Peters DC, Korosec FR, Grist TM, Block WF, Holden JE, Vigen KK, Mistretta CA. Undersampled projection reconstruction applied to MR angiography. Magn Reson Med 2000;43:91–101. [PubMed: 10642735]

[9]. Mistretta CA, Wieben O, Velikina J, Block WF, Perry J, Wu Y, Johnson K, Wu Y. Highly constrained backprojection for time-resolved MRI. Magn Reson Med 2006;55:30–40. [PubMed: 16342275]

[10]. O'Halloran RO, Wen Z, Holmes JH, Fain SB. Iterative Projection Reconstruction of Time-Resolved Images Using Highly Constrained Back-Projection (HYPR). MRM 2008;52:132–139.

[11]. Basser PJ, Matiello J, LeBihan D. MR Diffusion Tensor Spectroscopy and Imaging. Biophysical Journal 1994;66:259–267. [PubMed: 8130344]

[12]. Basser PJ. Relationships between Diffusion Tensor and *q*-space MRI. MRM 2002;47:392–397.

[13]. Balinov B, Jönsson B, Linse P, Söderman O. The NMR Self-Diffusion Method Applied to Restricted Diffusion. Simulation of Echo Attenuation from Molecules in Spheres and between Planes. JMR Series A 1993;104:17–25.

[14]. Blees MH. The effect of Finite Duration of Gradient Pulses on the Pulsed-Field-Gradient NMR Method for Studying Restricted Diffusion. JMR Series A 1994;109:203–209.

[15]. Mitra PP, Halperin BI. Effects of Finite Gradient-Pulse Widths in Pulsed-Field-Gradient Diffusion Measurements. JMR Series A 1995;113:94–101.

[16]. Chen XJ, Möller HE, Chawla MS, Cofer GP, Driehuys B, Hedlund LW, Johnson GA. Spatially Resolved Measurements of Hyperpolarized Gas Properties in the Lung In Vivo. Part I: Diffusion Coefficient. MRM 1999;42:721–728.

[17]. Schreider JP, Raabe OG. Structure of the Human Respiratory Acinus. AM J Anat 1981;162:221–232. [PubMed: 7315750]

[18]. Chen XJ, Hedlund LW, Möller HE, Chawla MS, Maronpot RR, Johnson GA. Detection of Emphysema in Rat Lungs by using Magnetic Resonance Measurements of He^3 Diffusion. PNAS 2000;97:11478–11481. [PubMed: 11027348]

[19]. Diaz S, Casselbrant I, Piitulainen E, Pettersson G, Magnusson P, Peterson B, Wollmer P, Leander P, Ekberg O, Akeson P. Hyperpolarized ^{3}He Apparent Diffusion Coefficient MRI of the Lung: Reproducibility and Volume Dependency in Healthy Volunteers and Patients with Emphysema. JMRI 2008;27:763–770. [PubMed: 18344208]

[20]. Carney DE, Bredenberg CE, Schiller HJ, Picone AL, McCann UG II, Gatto LA, Bailey G, Fillinger M, Nieman GF. The Mechanism of Lung Volume Change during Mechanical Ventilation. Am J Resp Care Med 1999;160:1697–1702.

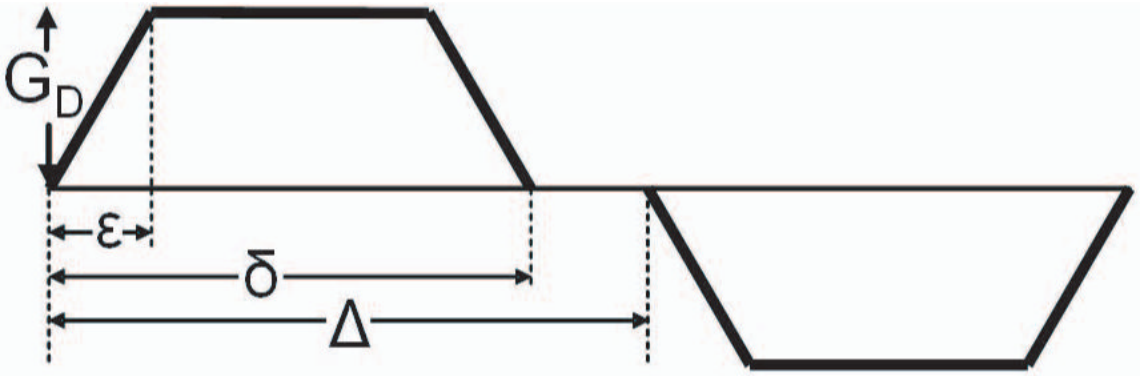

Figure 1.
The diffusion weighting gradient is a bipolar trapezoidal gradient with height, G_D, ramp time, ε, lobe time, δ, and diffusion time, Δ.

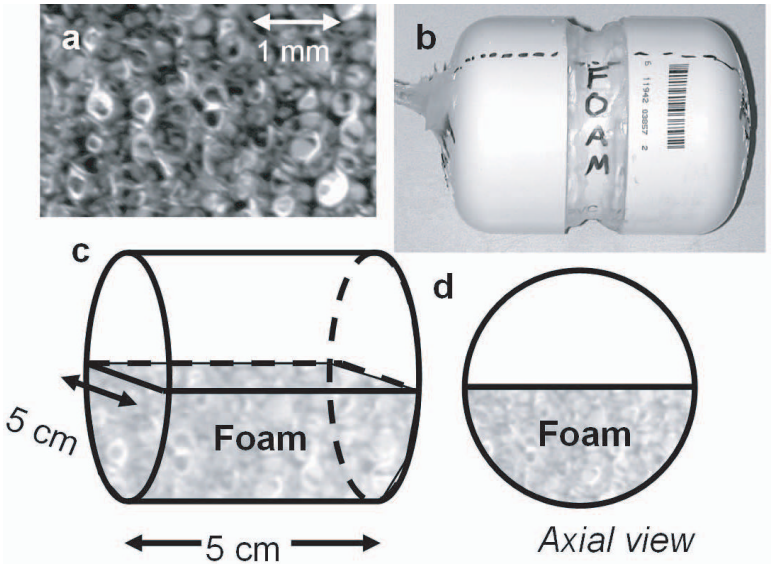

Figure 2.
Phantom 1 consisting of unrestricted and partially restricted regions. (a) A high resolution optical scan of the porous foam material used to construct the phantom. (b) A photograph of the exterior of the phantom with schematic diagrams (c,d) depicting the free diffusion region (c,d top) and the foam-containing region (c,d bottom).

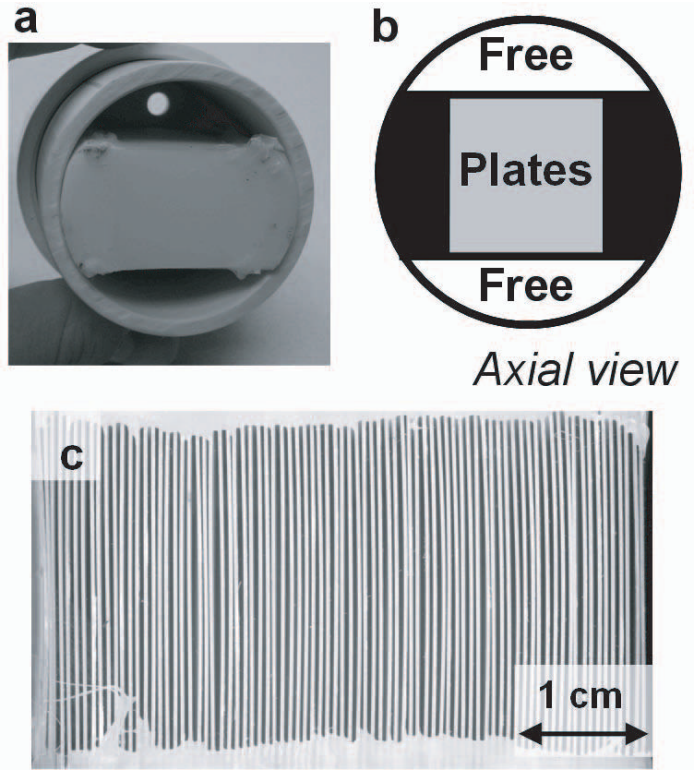

Figure 3.
Phantom 2 consisting of unrestricted and highly restricted regions. (a) A photograph of the inside of phantom before the second endcap was attached. 2. (b) A schematic diagram of the phantom corresponding to the view in the photograph in (a). (c) A high resolution optical scan of the parallel plates used in the phantom.

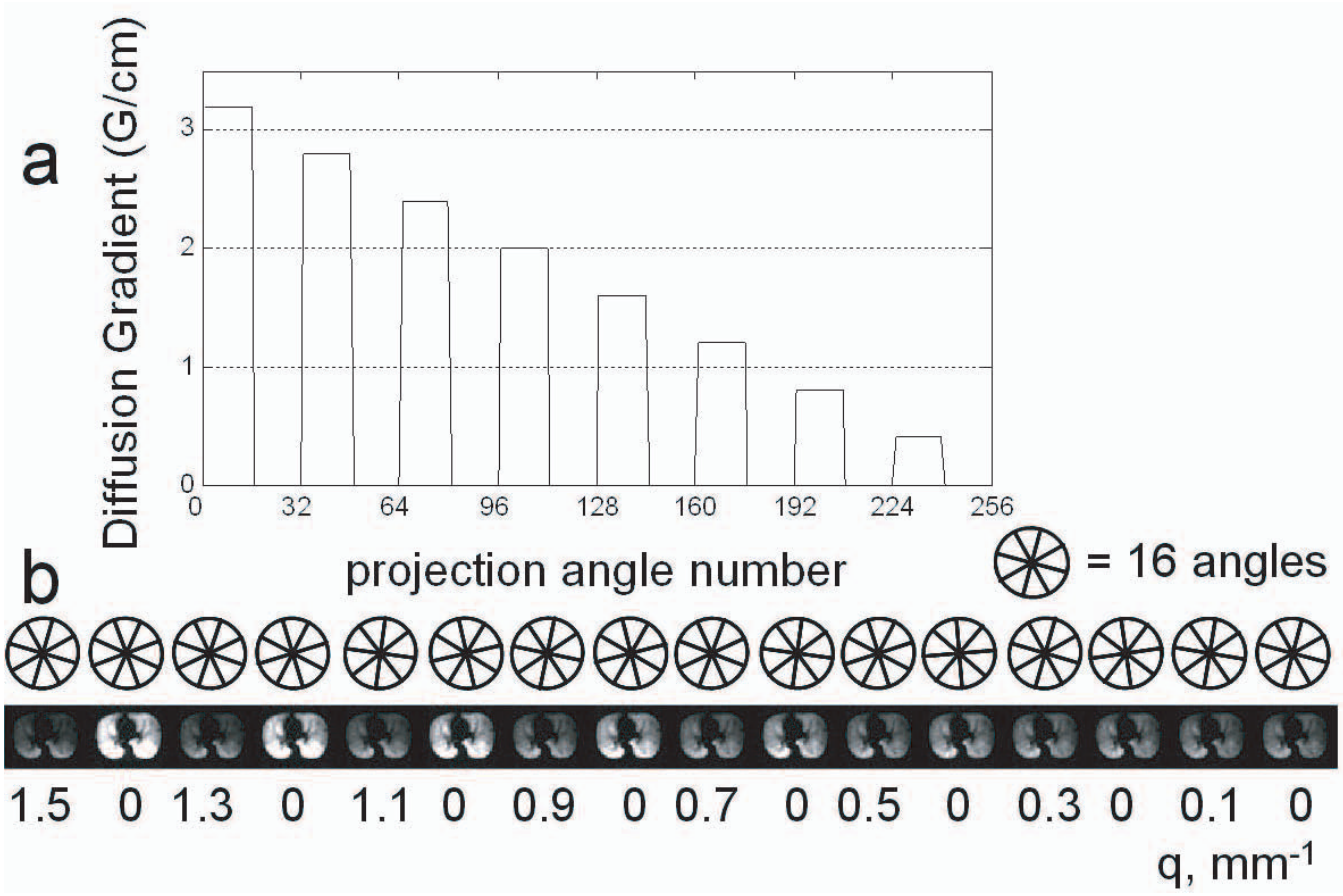

Figure 4.

(a) The maximum of the diffusion gradient as a function of projection number for each slice. Each group of 16 consecutively acquired angles shares a common diffusion weighting and were reconstructed to form a unique image. Note that there are 8 such groups with 0 diffusion weighting. These were reconstructed to form 8 unique unweighted images that were fitted to obtain the flip angle maps. Another representation of this (b) depicts the reconstructed image indexed by a q-value beneath the representation of the acquired angle set used to reconstruct that image.

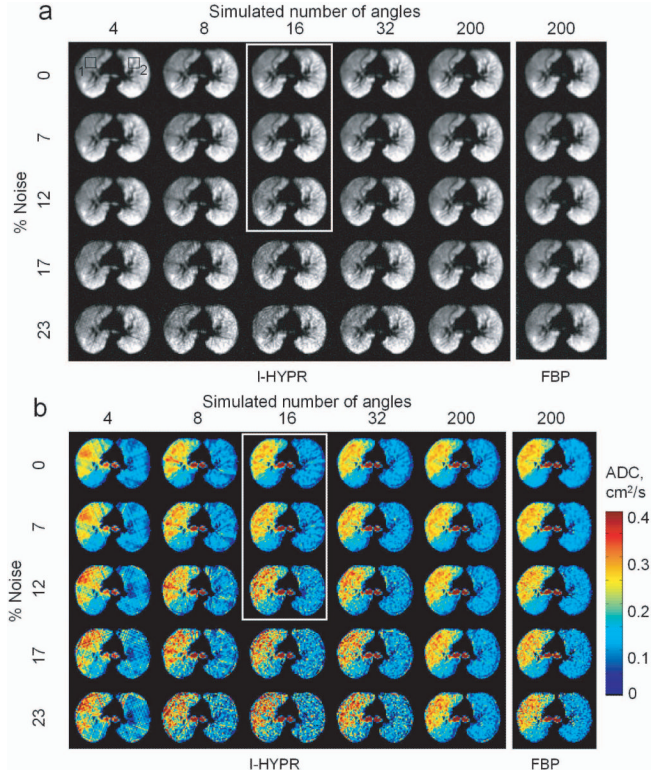

Figure 5.

(a) DW images reconstructed with I-HYPR compared to the respective FBP images for various noise levels (b) ADC maps calculated from simulated radial data using I-HYPR on the weighted image for a range of undersampling and added noise compared to the ideal ADC map. Note that as the number of projections increases from left to right that the apparent streak artifact is reduced. Also the I-HYPR reconstruction appears to be less sensitive to noise than the FBP reconstruction. Black squares labeled “1” and “2” in the upper left of (a) depict the location of ROIs 1 and 2 used in the ROI calculations presented in Table 1.

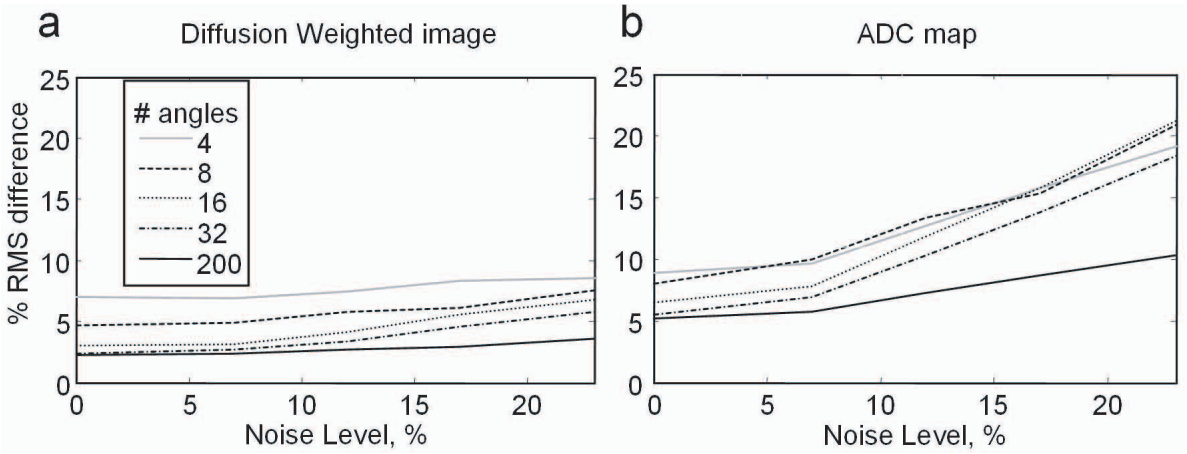

Figure 6.

(a) The RMS difference plotted versus noise level for the DW images reconstructed with angularly undersampled I-HYPR (with 4, 8, 15, 32, and 200 projection angles) and FBP using a fully sampled noise-free set of 200 angles. (b) The RMS difference between the ADC images calculated using I-HYPR-reconstructed images and fully sampled noise-free FBP images. Note that the increased error in the ADC map is due to the logarithm operation. Note there is residual error even for full angular sampling due to the inexact nature of the I-HYPR reconstruction.

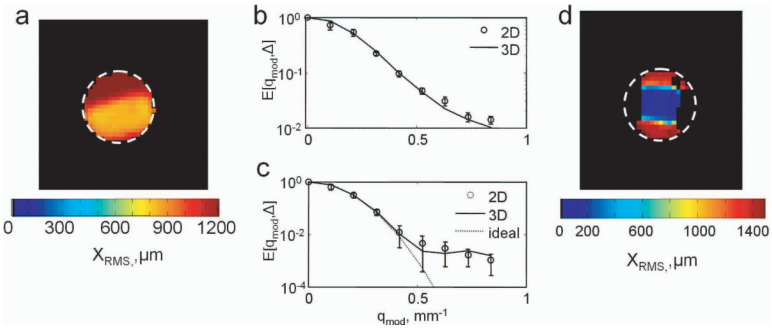

Figure 7.

(a) X_{RMS} map from phantom 1 showing the free diffusion region (upper) and the region of partially restricted diffusion in the porous foam (lower). (b) The measured normalized diffusion attenuated signal, $E[q_{mod}, \Delta]$, in the foam portion of phantom 1 compared for the Cartesian 2D (circles) and the undersampled 3D method of this work (line). (c) The expected signal attenuation for free Gaussian diffusion (dotted line) is compared to the 2D (circles) and 3D (solid line) measurements. Note the deviation from ideal when the noise floor is reached. (d) X_{RMS} map from phantom 2 showing the highly restricted diffusion region of the parallel plates (center, blue) and the free diffusion regions (above and below, red). In both (a) and (d) a white dotted line indicates the approximate position of the inner wall of the phantom.

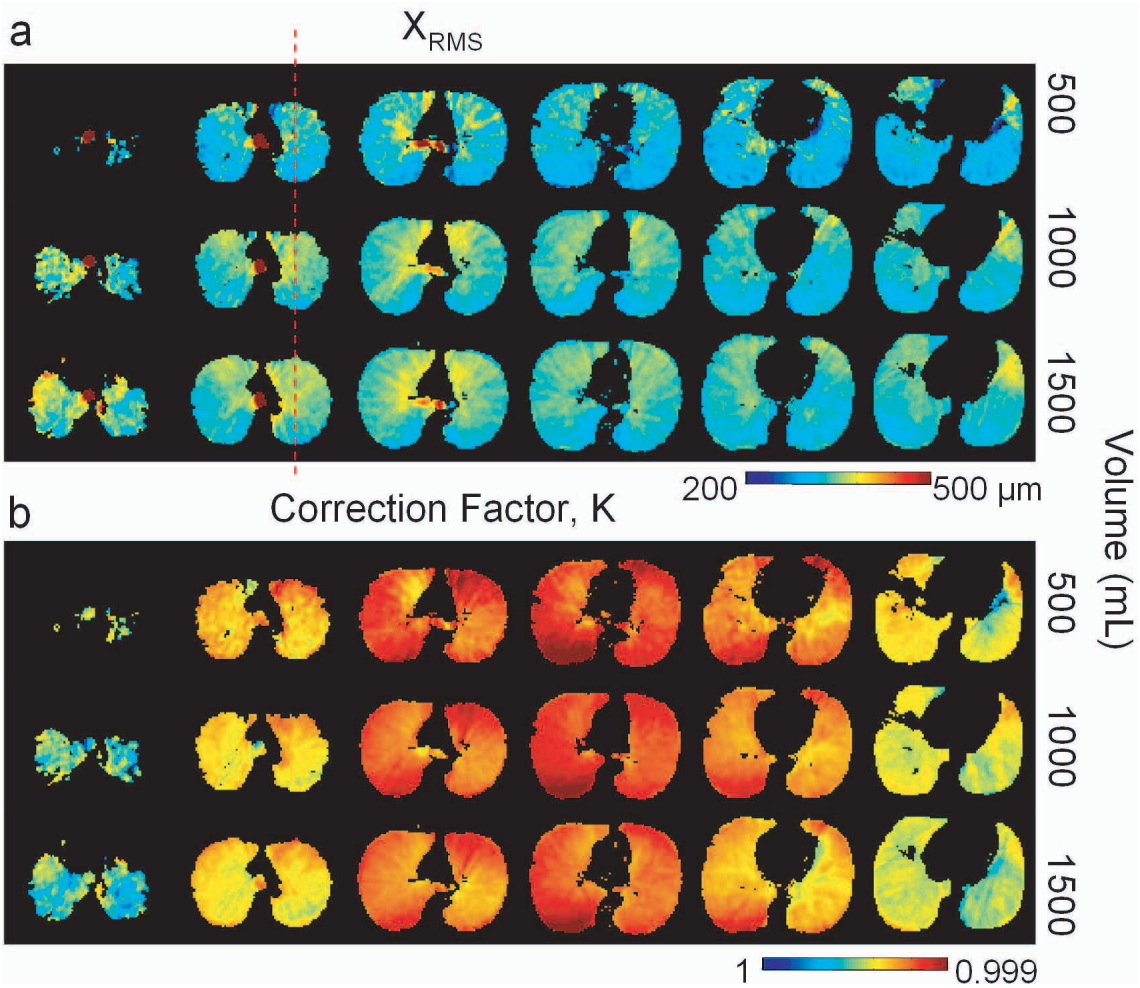

Figure 8.

Normal human volunteer study showing (a) X_{RMS} and correction maps from the three inhaled volumes are compared. Note the dependence of X_{RMS} on the apical to basal location and on the anterior to posterior location. (b) The correction maps for all the images are compared and appear to be qualitatively similar. The differences are likely due to the effect of the volume change on the flexible coil. Note that the dashed red line (a) indicates the location of the profiles plotted in Fig 9c.

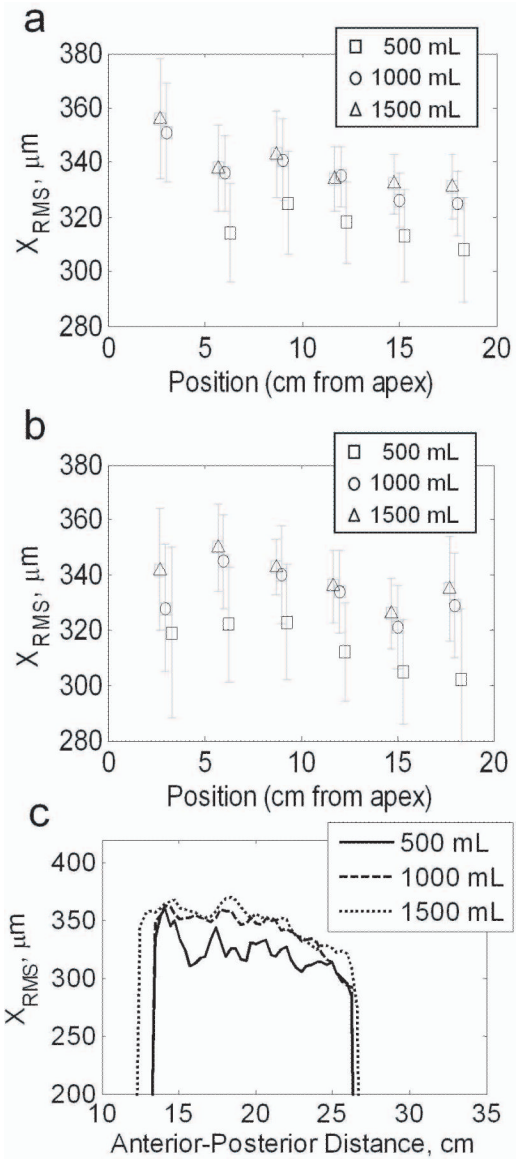

Figure 9.

Lung volume measures of average X_{RMS} values from the human volunteer for ROI's encompassing the entire left (a) and right (b) lungs depict the expected apical to basal dependence of structure size. Also the increase in X_{RMS} with inhaled volume can be seen. (c) Anterior to posterior profiles for are compared for each inhaled volume. The anterior to posterior gradient is apparent for each inhaled volume.

Magn Reson Med. Author manuscript; available in PMC 2010 April 26.

Table 1

ROI measurements for the computer simulation.The mean value in the ROI is reported with the standard deviation in parentheses. The top half of the table gives ROI measurements in the DW images and the lower half gives the ROI measurements in the ADC images.

		DW Images (au)					
		Angles	I-HYPR				FBP
Noise %		4	8	16	32	200	200
	0	92 (10)	94 (11)	93 (11)	94 (11)	94 (11)	93 (10)
	7	91 (11)	93 (12)	92 (12)	93 (11)	93 (11)	93 (10)
ROI 1	12	93 (12)	93 (14)	92 (16)	92 (13)	93 (12)	93 (10)
	17	90 (13)	90 (17)	93 (20)	91 (16)	93 (13)	93 (11)
	23	93 (18)	92 (22)	92 (18)	91 (21)	92 (14)	93 (12)
	0	141 (31)	142 (33)	141 (32)	141 (33)	141 (33)	140 (29)
	7	141 (31)	141 (34)	140 (32)	140 (34)	140 (33)	140 (29)
ROI 2	12	141 (32)	140 (34)	141 (36)	139 (34)	140 (34)	141 (30)
	17	139 (31)	140 (35)	138 (36)	140 (37)	140 (33)	140 (29)
	23	140 (33)	140 (36)	138 (40)	139 (38)	139 (33)	140 (29)
		ADC (cm2/s)					
	0	0.26 (0.03)	0.26 (0.03)	0.26 (0.03)	0.26 (0.02)	0.26 (0.02)	0.26 (0.02)
	7	0.27 (0.04)	0.26 (0.04)	0.27 (0.03)	0.27 (0.03)	0.26 (0.02)	0.26 (0.02)
ROI 1	12	0.26 (0.04)	0.27 (0.05)	0.27 (0.06)	0.27 (0.05)	0.27 (0.03)	0.27 (0.03)
	17	0.28 (0.05)	0.28 (0.07)	0.27 (0.08)	0.28 (0.06)	0.27 (0.03)	0.26 (0.04)
	23	0.27 (0.07)	0.28 (0.09)	0.27 (0.09)	0.28 (0.08)	0.27 (0.04)	0.26 (0.05)
	0	0.11 (0.02)	0.11 (0.02)	0.11 (0.02)	0.11 (0.02)	0.11 (0.03)	0.11 (0.02)
	7	0.11 (0.03)	0.11 (0.03)	0.11 (0.03)	0.12 (0.03)	0.11 (0.03)	0.11 (0.02)
ROI 2	12	0.11 (0.03)	0.11 (0.03)	0.11 (0.05)	0.12 (0.04)	0.11 (0.03)	0.11 (0.02)
	17	0.12 (0.04)	0.12 (0.05)	0.12 (0.05)	0.12 (0.05)	0.11 (0.03)	0.11 (0.03)
	23	0.11 (0.05)	0.11 (0.07)	0.12 (0.06)	0.12 (0.06)	0.12 (0.04)	0.11 (0.04)

Table 2

Summary of Phantom Experiments.

Phantom 1 (Foam)			
	2D	**3D**	**Ideal**
X_{RMS} foam (μm)	800 (100)	840 (10)	n/a†
X_{RMS} free (μm)	1200 (200)	1170(10)	1140
Phantom 2 (Parallel Plates)			
X_{RMS} plates (μm)		126 (40)	118‡
X_{RMS} free (μm)		1390 (80)	1320

† Due to the complex structure of the foam phantom no ideal X_{RMS} value can be determined.

‡ This is the X_{RMS} value expected for a 290 μm gap with infinitely impermeable walls.

Table 3

Summary of Human Experiments.

	Human Volunteer (inhaled volume)			
	500 mL	**1000 mL**	**1500 mL**	**Ideal**
X_{RMS} whole lung (μm)	320 (40)	340 (30)	340 (30)	
X_{RMS} Trachea (μm)	780 (40)	790 (60)	780 (40)	774